Self-noise prediction of a flat plate using a hybrid RANS-BEM technique

P. Croaker[1], N. Kessissoglou[1], M. Karimi[1], C. Doolan[2] and L. Chen[3]

[1] School of Mechanical & Manufacturing Engineering, UNSW Australia, Sydney, Australia

[2] School of Mechanical Engineering, the University of Adelaide, Adelaide, Australia

[3] Maritime Division, Defence Science and Technology Organisation, Melbourne, Australia

ABSTRACT

The self-noise generated by a flat plate immersed in low Mach number flow is predicted using a hybrid RANS-BEM technique. A Reynolds Averaged Navier-Stokes (RANS) simulation is performed of the turbulent flow over the flat plate. The predicted flow field data, such as mean velocity, turbulent kinetic energy and turbulent dissipation rate, is then processed using a statistical noise model and combined with a boundary element method (BEM) model of the flat plate to predict the far-field sound. The results from the hybrid RANS-BEM technique are presented for turbulent flow past a flat plate, with Reynolds number based on chord Re_c=2.0 $\times$ 10^5 and Mach number M=0.044. The computed aerodynamic and acoustic results are compared with numerical and experimental results from the literature.

Keywords: Computational fluid dynamics, flow induced noise, boundary element method
I-INCE Classification of Subjects Number(s): 21.6.4

1. INTRODUCTION

Lighthill (1, 2) reformulated the Navier-Stokes equation into a wave equation that represents the acoustic source generation by fluid motion and the propagation of these acoustic sources. He derived an acoustic analogy that demonstrates sound generated by a turbulent fluid flow is equivalent to the sound generated by a distribution of acoustic quadrupoles computed from the instantaneous velocity fluctuations. Curle (3) extended Lighthill's acoustic analogy to include the effect of stationary boundaries present in the turbulent flow on the sound generation. He showed that the contribution of a stationary rigid body on the sound generated by unsteady flow is equivalent to a surface distribution of acoustic dipoles computed from the instantaneous pressure fluctuations on the body.

An important result from Lighthill's work is that the acoustic source terms can be calculated from hydrodynamic flow field variables. This has prompted the development of a wide range of hybrid methods that use computational fluid dynamics (CFD) to calculate acoustic source terms from transient flow variables and Lighthill's acoustic analogy to predict the acoustic source propagation. These hybrid methods typically make use of the Green's function solution of the wave equation to reformulate the acoustic propagation problem into a boundary integral equation. The most common approach is to employ a free-field Green's function or its spatial derivatives to predict the propagation of the acoustic waves. These free-field Green's functions do not directly account for the influence of solid bodies on the acoustic wave propagation. Hence, if solid bodies are present, Curle's (or a similar) analogy must be used. However, it is possible to use a hard-wall, or geometry-tailored, Green's function which explicitly includes the presence of the rigid bodies on the wave propagation. In such cases, only the volumetric acoustic sources derived by Lighthill are required because the hard-walled Green's function automatically accounts for the scattering and diffraction of acoustic waves by the body (4, 5). For certain applications, a suitable approximation to the hard-wall Green's function can be made, such as using the Green's function of a semi-infinite plane to approximate the hard-wall boundary of an airfoil's trailing edge (6, 7). For more complex geometries, such approximations no longer hold and the hard-wall Green's function must be numerically predicted using boundary element methods (8). The boundary element method (BEM) is particularly well suited to model acoustic propagation in an exterior unbounded fluid because the BEM formulation automatically satisfies the Sommerfeld radiation condition.

[1] p.croaker@unsw.edu.au

Ffowcs Williams and Hall (6) considered the case of turbulent eddies convecting past a sharp edge, such as encountered at the trailing edge of a hydrofoil. A theoretical model based on a vanishingly thin half plane of infinite extent was developed. The acoustic waves emitted from a volume quadrupole source and the interaction of these waves with a rigid half plane was considered. They showed that the far-field sound intensity for trailing edge noise had a scaling of M^5 and identified that the mechanism responsible for this trailing edge noise was the scattering and diffraction of the flow induced acoustic waves by the thin trailing edge. Furthermore, they concluded that this trailing edge noise must be the dominant source of noise generated by marine vessels based purely on the low Mach numbers encountered in marine applications.

Flow induced noise generated by a marine vessel is characterised by low Mach number flows with very high Reynolds numbers and presents unique challenges to flow induced noise modelling. Accurately resolving wall-bounded flow at very high Reynolds numbers requires a high fidelity mesh. Computing the time resolved hydrodynamics on this mesh is a computationally demanding task in terms of data storage and simulation time. Hence transient hydrodynamic simulation techniques, such as unsteady RANS, large eddy simulation (LES) or direct numerical simulation (DNS) are impractical for hydroacoustic flow noise predictions of full scale marine vessels. An attractive alternative is to develop noise models based on the turbulence statistics available from a steady-state RANS simulation. Such RANS based techniques require a method to predict fluctuating flow noise sources from the average flow quantities obtained from the RANS simulation. The stochastic noise generation and radiation model (SNGR) is a RANS based technique where a prescribed two-point turbulence statistics is applied to spatially filtered white noise to create a synthetic turbulence field (9). This synthetic turbulence field is then applied to a linearised Euler equation solver to predict the propagation of the acoustic waves, interaction with acoustically hard surfaces and the resulting far-field radiated sound. The SNGR method has successfully been applied to predict the sound generated by turbulent flow past a trailing edge (9, 10, 11). However the generation of the synthetic turbulence field is computationally demanding (12). Another approach is to use a trailing edge noise model that predicts the far-field sound based on the surface pressure spectrum near the trailing edge (13, 14). Lee et al. (15) developed a technique to predict the surface pressure spectra from RANS mean flow data. Albarracin et al. (12) state that these surface pressure based RANS flow noise models assume homogeneity of the turbulence in the spanwise and chordwise directions. For trailing edge flows where there is an adverse pressure gradient, or spanwise variation in trailing edge geometry, this assumption of homogeneous turbulence is not valid. Albarracin et al. (12) proposed a RANS-based statistical noise model (RSNM) that uses an assumed turbulent velocity cross spectrum defined in terms of RANS mean flow data to characterise the flow noise sources in the boundary layer. The turbulent velocity cross spectra are then combined with a Green's function for a semi-infinite half-plane to predict the scattering and diffraction of sound by the trailing edge. The model of Albarracin et al. (12) does not make any assumption regarding the homogeneity of the turbulence.

Many of the control surfaces and appendages of a marine vessel have relatively thick profiles and are not well represented by a vanishingly thin plane. To accurately resolve the scattering and diffraction from such appendages requires a technique such as the boundary element method. Ostertag et al. (16) developed a BEM technique to predict flow induced noise from RANS data. Monopole sources were placed at each field point location and the acoustic pressure at each source point was recorded. The double spatial derivative of the pressure at the source points were calculated and the reciprocal theorem was used to determine the tailored Green's function of the body. This approach relies on taking the double spatial derivative of a volume distribution of acoustic pressures to determine the tailored Green's function. Significant errors can be introduced by spatial discretisation and differentiation on a numerical grid (17).

This paper presents a hybrid RANS-BEM technique to predict flow induced noise produced by turbulent flow past a body. The flow noise sources are modelled using the RANS-based statistical noise model (RSNM) technique developed by Albarracin et al. (12). The incident acoustic field produced by these statistical flow noise sources are then calculated and applied to a BEM-based prediction of the scattering and diffraction. The spatial derivatives are applied to the Green's functions instead of the flow noise sources, hence avoiding any errors associated with numerical differentiation. The hybrid RANS-BEM technique is applied to predict the far-field sound produced by turbulent flow over a flat plate with Reynolds number based on the chord Re_c=2.0 $\times$ 10^5 and Mach number M=0.044.

2. NUMERICAL PROCEDURE

2.1 Incident Pressure From a Single Turbulent Source

To determine the far-field pressure from a single turbulent source (for example, a single CFD cell), the incident pressure on the body is calculated using:

$$p^*_{c,inc}(\mathbf{x},\omega) = \int_{\Omega_c} (\rho U_{i,c} U_{j,c})^* \frac{\partial^2 G_h(\mathbf{x},\mathbf{y})}{\partial y_i \partial y_j} d\Omega_c \tag{1}$$

where $p^*_{c,inc}(\mathbf{x},\omega)$ is the Fourier transform of the incident pressure at field point $\mathbf{x}$ and angular frequency ω due to the c^{th} CFD cell. ρ is the density of the fluid $U_{i,c}$ is the fluid velocity in the i^{th} direction at CFD cell c and consists of a mean component $\bar{U}_{i,c}$ and a fluctuating $u'_{i,c}$ component as follows

$$U_{i,c} = \bar{U}_{i,c} + u'_{i,c} \tag{2}$$

Ω_c is the computational domain occupied by the c^{th} CFD cell. $G_h(\mathbf{x},\mathbf{y}) = \frac{e^{\tilde{i}k_a r}}{4\pi r}$ is the harmonic free-field Green's function. k_a is the acoustic wave number, $r = \|\mathbf{x}-\mathbf{y}\|$ is the distance between the source and field points and $\tilde{i} = \sqrt{-1}$. Initially considering only two dimensions, assuming the fluid is incompressible and that the velocity is constant over Ω_c, equation (1) is represented by

$$\begin{aligned} p^*_{c,inc}(\mathbf{x},\omega) &= \rho_0 \left(U^2_{1,c}\right)^* \int_{\Omega_c} \frac{\partial^2 G_h(\mathbf{x},\mathbf{y})}{\partial y_1^2} d\Omega_c + 2\rho_0 \left(U_{1,c}U_{2,c}\right)^* \int_{\Omega_c} \frac{\partial^2 G_h(\mathbf{x},\mathbf{y})}{\partial y_1 \partial y_2} d\Omega_c \\ &\quad + \rho_0 \left(U^2_{2,c}\right)^* \int_{\Omega_c} \frac{\partial^2 G_h(\mathbf{x},\mathbf{y})}{\partial y_2^2} d\Omega_c \end{aligned} \tag{3}$$

where ρ_0 is the density of the fluid at rest. Using the following approximations (6)

$$\begin{aligned} \left(U^2_{1,c}\right)^* &\approx 2\bar{U}_{1,c} u'^*_{1,c} \\ \left(U^2_{2,c}\right)^* &\approx 2\bar{U}_{2,c} u'^*_{2,c} \\ \left(U_{1,c}U_{2,c}\right)^* &\approx \bar{U}_{1,c} u'^*_{2,c} + \bar{U}_{2,c} u'^*_{1,c} \end{aligned} \tag{4}$$

equation (3) can then be expressed as

$$\begin{aligned} p^*_{c,inc}(\mathbf{x},\omega) &= 2\rho_0 \bar{U}_{1,c} u'^*_{1,c} \int_{\Omega_c} \frac{\partial^2 G_h(\mathbf{x},\mathbf{y})}{\partial y_1^2} d\Omega_c + 2\rho_0 \left(\bar{U}_{1,c} u'^*_{2,c} + \bar{U}_{2,c} u'^*_{1,c}\right) \int_{\Omega_c} \frac{\partial^2 G_h(\mathbf{x},\mathbf{y})}{\partial y_1 \partial y_2} d\Omega_c \\ &\quad + 2\rho_0 \bar{U}_{2,c} u'^*_{2,c} \int_{\Omega_c} \frac{\partial^2 G_h(\mathbf{x},\mathbf{y})}{\partial y_2^2} d\Omega_c \end{aligned} \tag{5}$$

Introducing an anisotropy factor f_a and assuming that the fluctuating velocity components are related to each other as follows

$$u'^*_{1,c} = f_a u'^*_{2,c} \tag{6}$$

allows equation (5) to be represented by

$$\begin{aligned} p^*_{c,inc}(\mathbf{x},\omega) &= 2\rho_0 u'^*_{2,c} \left(f_a \bar{U}_{1,c} \int_{\Omega_c} \frac{\partial^2 G_h(\mathbf{x},\mathbf{y})}{\partial y_1^2} d\Omega_c + \left(\bar{U}_{1,c} + f_a \bar{U}_{2,c}\right) \int_{\Omega_c} \frac{\partial^2 G_h(\mathbf{x},\mathbf{y})}{\partial y_1 \partial y_2} d\Omega_c \right. \\ &\quad \left. + \bar{U}_{2,c} \int_{\Omega_c} \frac{\partial^2 G_h(\mathbf{x},\mathbf{y})}{\partial y_2^2} d\Omega_c \right) \end{aligned} \tag{7}$$

Dividing both sides of equation (7) by $u'^*_{2,c}/U_{\text{con}}$ (where U_{con} is the convection velocity) yields the following expression

$$p^{\dagger *}_{c,inc}(\mathbf{x},\omega) = U_{\text{con}} \frac{p^*_c(\mathbf{x},\omega)}{u'_2(\mathbf{y})^*} \tag{8}$$

$$\begin{aligned} &= 2\rho_0 U_{\text{con}} \left(f_a \bar{U}_{1,c} \int_{\Omega_c} \frac{\partial^2 G_h(\mathbf{x},\mathbf{y})}{\partial y_1^2} d\Omega_c + \left(\bar{U}_{1,c} + f_a \bar{U}_{2,c}\right) \int_{\Omega_c} \frac{\partial^2 G_h(\mathbf{x},\mathbf{y})}{\partial y_1 \partial y_2} d\Omega_c \right. \\ &\quad \left. + \bar{U}_{2,c} \int_{\Omega_c} \frac{\partial^2 G_h(\mathbf{x},\mathbf{y})}{\partial y_2^2} d\Omega_c \right) \end{aligned} \tag{9}$$

where $p^{\dagger *}_{c,inc}(\mathbf{x},\omega)$ is the incident pressure normalised by the ratio of the fluctuating velocity of cell c to the convection velocity.

2.2 Scattered Pressure Field Using the BEM

The non-homogeneous Helmholtz equation is given by (18)

$$\triangle p_a^*(\mathbf{x},\omega)+k_a^2 p_a^*(\mathbf{x},\omega)=-Q \tag{10}$$

where $p_a^*(\mathbf{x},\omega)$ is the acoustic pressure at field point $\mathbf{x}$ and Q is an acoustic source. As described by Marburg and Nolte (18), a solution of the non-homogeneous Helmholtz equation can be obtained by calculating the incident pressure on the body radiated by the source and applying it as a load to the boundary integral equation as follows

$$\begin{aligned} c(\mathbf{y})\,p_a^*(\mathbf{y},\omega) &= -\int_\Gamma \frac{\partial G_h(\mathbf{x},\mathbf{y})}{\partial n(\mathbf{x})} p_a^*(\mathbf{x},\omega)\,d\Gamma(\mathbf{x}) \\ &\quad +\tilde{i}\rho_0 c_0 k_a \int_\Gamma G_h(\mathbf{x},\mathbf{y})\,v_a^*(\mathbf{x},\omega)\,d\Gamma(\mathbf{x})+p_{a,inc}^*(\mathbf{y},\omega) \end{aligned} \tag{11}$$

$p_{a,inc}^*(\mathbf{y},\omega)$ is the pressure incident on the boundary Γ as a result of the acoustic source. $c(\mathbf{y})$ is a free-term coefficient equal to 1 in the domain interior and 0.5 on a smooth boundary. n is a unit vector in the direction normal to the boundary and v_a is the fluid particle velocity. For the hybrid RANS-BEM approach, the velocity normalised pressure $p_{c,inc}^{\dagger *}(\mathbf{x},\omega)$ is substituted into equation (11) to yield

$$\begin{aligned} c(\mathbf{y})\,p_c^{\dagger *}(\mathbf{y},\omega) &= -\int_\Gamma \frac{\partial G_h(\mathbf{x},\mathbf{y})}{\partial n(\mathbf{x})} p_c^{\dagger *}(\mathbf{x},\omega)\,d\Gamma(\mathbf{x}) \\ &\quad +\tilde{i}\rho_0 c_0 k_a \int_\Gamma G_h(\mathbf{x},\mathbf{y})\,v_c^{\dagger}(\mathbf{x},\omega)\,d\Gamma(\mathbf{x})+p_{c,inc}^{\dagger *}(\mathbf{y},\omega) \end{aligned} \tag{12}$$

where $p_c^{\dagger *}$ is velocity normalised scattered pressure on the body due to the flow noise source in the c^{th} CFD cell. $p_{c,inc}^{\dagger *}(\mathbf{y},\omega)$ is the velocity normalised incident pressure due to the c^{th} CFD cell, calculated in the preceding section and $v_c^{\dagger}(\mathbf{x},\omega)$ is the velocity normalised particle velocity on the body arising from the flow noise sources in CFD cell c. Solving equation (12) will predict the distribution of velocity normalised pressure $p_c^{\dagger *}(\mathbf{y},\omega)$ over the body that occurs when the incident field interacts with the geometry of the body, with the normal derivative of the normalised pressure constrained to zero on the body (for a rigid body).

The velocity normalised pressure in the far-field $p_c^{\dagger *}(\mathbf{x_f},\omega)$ due to the flow noise source in the c^{th} CFD cell can be determined by solving

$$p_c^{\dagger *}(\mathbf{x_f},\omega)=-\int_\Gamma \frac{\partial G_h(\mathbf{x},\mathbf{y})}{\partial n(\mathbf{x})} p_c^{\dagger *}(\mathbf{x},\omega)\,d\Gamma(\mathbf{x}) \tag{13}$$

The far-field pressure $p_c^*(\mathbf{x_f},\omega)$ can then be expressed as

$$p_c^*(\mathbf{x_f},\omega)=\frac{u_{2,c}^*}{U_{\text{con}}} p_c^{\dagger *}(\mathbf{x_f},\omega) \tag{14}$$

The scattered fields were obtained using the AEBEM2 subroutine of Kirkup (19). AEBEM2 is a two-dimensional solver and the scattered pressure calculated by the subroutine must then be converted from two dimensions to three dimensions. The following technique of Oberai et al. (20) is used to convert the two-dimensional pressure calculated by AEBEM2 into three-dimensional pressure

$$p_{c,3D}^*(\mathbf{x_f},\omega)\approx p_c^*(\mathbf{x_f},\omega)\,\frac{1+\tilde{i}}{2}\sqrt{\frac{k_a}{\pi r}} \tag{15}$$

where $p_c^*(\mathbf{x_f},\omega)$ and $p_{c,3D}^*(\mathbf{x_f},\omega)$ are respectively the two and three-dimensional far-field pressures produced by the c^{th} CFD cell at angular frequency ω.

2.3 Far-field Power Spectral Density

The power spectral density (PSD) $S(\mathbf{x_f},\omega)$ at the far-field point $\mathbf{x_f}$ is calculated by the double summation as follows

$$S(\mathbf{x_f},\omega)=\sum_{b=1}^{M}\sum_{c=1}^{M} p_{b,3D}^*(\mathbf{x_f},\omega)\,\hat{p}_{c,3D}^*(\mathbf{x_f},\omega) \tag{16}$$

where M is the total number of CFD cells. Substituting equation (8) into equation (16) yields

$$S(\mathbf{x_f},\omega) = \sum_{b=1}^{M}\sum_{c=1}^{M} \frac{\left[u_{2,b}^{*}\hat{u}_{2,c}^{*}\right]}{U_{\mathrm{con}}^{2}} \left[p_b^{\dagger *}(\mathbf{x_f},\omega)\,\hat{p}_c^{\dagger *}(\mathbf{x_f},\omega)\right] \tag{17}$$

where $\left[u_{2,b}^{*}\,\hat{u}_{2,c}^{*}\right]$ is the turbulent velocity cross spectrum

$$\Phi(b,c,\omega) = \left[u_{2,b}^{*}\,\hat{u}_{2,c}^{*}\right] \tag{18}$$

and is the only unknown quantity in the model. It is possible to measure this turbulent velocity cross spectrum experimentally, predict it numerically from a transient fluid dynamics simulation or to apply an analytical or empirical model to describe the turbulent velocity cross spectrum. In this work, an analytical model is applied and is described in the proceeding section.

2.4 Turbulent velocity cross spectrum

Following the work of Albarracin et al. (12), the turbulent velocity cross-spectrum is represented as

$$\Phi(b,c,\omega) = \frac{A\sqrt{\pi}}{\omega_s} u_s^2 \exp\left(-\frac{|\mathbf{y}_c-\mathbf{y}_b|^2}{l_s^2}\right) \exp\left(-\frac{\omega^2}{4\omega_s^2}\right) \tag{19}$$

where u_s is the characteristic velocity, ω_s is the characteristic frequency and l_s is the characteristic length scale of the turbulence associated with each CFD cell. The model parameters are linked to the RANS turbulence data using the following (12)

$$u_s = \sqrt{2k/3}, \qquad \omega_s = 2\pi/\tau_s, \qquad \tau_s = c_\tau k/\varepsilon, \qquad l_s = c_l k^{3/2}/\varepsilon \tag{20}$$

where k is the turbulent kinetic energy, ε is the turbulent dissipation rate and c_l, c_τ are semi-empirical parameters. Albarracin et al. (12) determined that $c_l = 0.11$ and $c_\tau = 0.012U_\infty + 0.73$ where U_∞ is the free stream velocity. For the case considered here, a correlation strength parameter of $A = 1/6300$ was required to produce good agreement between numerical and experimental results.

2.5 CFD Model

A sharp-edged flat plate with a chord of 200 mm and a thickness of 5 mm was modelled. The leading edge was circular with a diameter of 5 mm while the trailing edge was a symmetric wedge shape with an apex angle of 12 degrees. Moreau et al. (21, 22) conducted experiments on the same plate in the University of Adelaide's anechoic wind tunnel. Their experimental measurements are used to validate the numerical models and results presented in this paper. In the experiment, the flat plate had a span of 450 mm, however a two-dimensional CFD simulation was performed in the present work. Incompressible flow field past the flat plate is simulated at a Reynolds number based on chord Re_c=2.0 $\times$ 10^5 and Mach number M=0.044. The two-dimensional steady RANS simulation was performed in Fluent on a C-grid domain with approximately 1.0×10^5 quadrilateral cells. The computational domain extends for two chord lengths above and below the plate as well as upstream of the leading edge. Downsteam of the trailing edge the computational domain extends for an additional three chord lengths. The boundary layer mesh is well resolved, with $y^+ \sim 1$ for the cells immediately adjacent to the plate.

The inlet velocity was set to 15 m/s on the semi-circular boundary, with a turbulence intensity of 0.3% which matches the turbulence intensity at the inflow plane of the experimental facility at the University of Adelaide (22). A zero average pressure boundary condition was imposed at the outlet. A no-slip condition was applied on the surface of the plate, and the top and bottom boundaries are considered as free-slip walls. The $k-\omega$ SST turbulence model was applied, with a low inflow turbulence intensity specified. Figure 1 shows the mesh resolution used in the vicinity of the trailing edge.

2.6 BEM Model

The two-dimensional BEM model consisted of 180 linear one-dimensional boundary elements distributed around the flat plate. A greater concentration of boundary elements were placed around the leading edge and along the tapered wedge at the trailing edge to ensure that interaction of the incident field with the geometry of the plate is accurately captured. The vertices of these BEM elements also represent the field points used to calculate the incident normalised pressure using equation (9). The AEBEM2 subroutine of Kirkup (19) was used to solve equation (12) to predict the scattered normalised pressure. Equations (9) and (12) must be solved

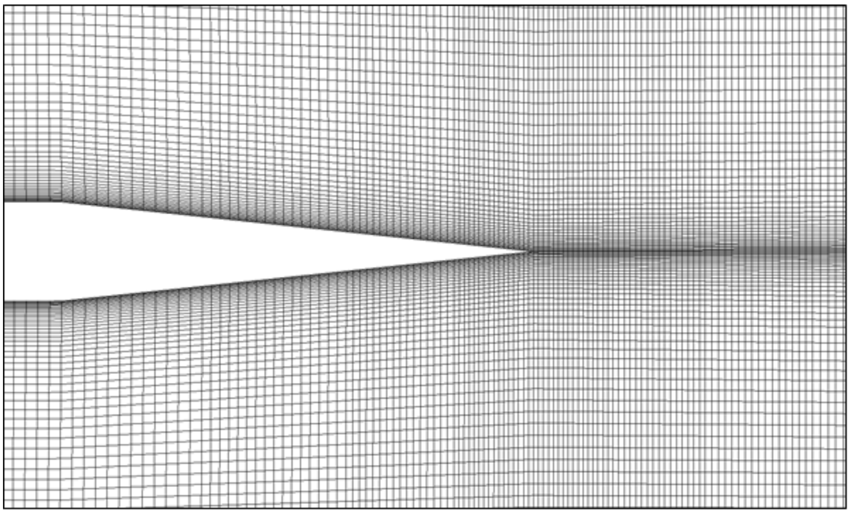

Figure 1 – CFD mesh near trailing edge of the plate

once for each CFD cell. The far-field power spectral density is then calculated by solving equation (17). This suggests that a separate BEM solution is required for every CFD cell which would render the proposed method incredibly inefficient. However, this is not the case. The BEM matrices must be inverted only once for all CFD cells. The scattered far-field pressures produced by each CFD cell are then obtained by performing an efficient matrix multiplication of the inverted BEM matrices with the incident normalised pressure.

3. RESULTS

3.1 Turbulent Flow Field

Figure 2 shows the turbulent kinetic energy (a) and turbulent dissipation rate (b) predicted for the sharp-edged flat plate. All contours are shown on a log scale to highlight the main features. Figure 2 reveals that immediately downstream of the rounded leading edge, a region of high turbulent kinetic energy and dissipation occurs. The rounded leading edge causes the flow to separate and a laminar separation bubble forms (22). The resulting separated shear layer generates a significant amount of turbulence which is then transported along the plate and convected past the sharp trailing edge. Figure 3 compares the normalised mean $\bar{U}/U_\infty$ and root mean square (rms) velocity $u'_{\mathrm{rms}}/U_\infty$ obtained from the present RANS simulation with the experimental measurements of Moreau et al. (22). The mean flow in the near wake is well predicted using the present two-dimensional RANS simulation. Figure 3(b) shows some slight discrepancy between the predicted and measured u'_{rms}. For a Reynolds number based on chord of $Re_c = 2.0 \times 10^5$, the flow is in the turbulent unsteady regime and the flow structures are three dimensional. The present two-dimensional RANS simulation assumes that there is no spanwise variation in the flow field and this may contribute to the observed discrepancy in the u'_{rms} prediction. Also, the current CFD model only extends three chord lengths downstream of the trailing edge and this truncation of the flow domain may adversely effect the upstream flow field. Nevertheless, good agreement between the RANS simulation and the experimental measurements is obtained.

Based on the turbulent kinetic energy and dissipation rate, as well as using the values for the parameters $c_l = 0.11$ and $c_\tau = 0.012U_\infty + 0.73$, the distribution of characteristic velocity u_s, characteristic frequency ω_s and characteristic length l_s used in the RANS-based statistical noise model are calculated. Figure 4 shows the characteristic velocity u_s, the characteristic frequency ω_s and the characteristic length scale l_s around the flat plate, with the contours displayed on a log scale to show the vast range of scales present in the model. The distribution of the characteristic velocity u_s reveals that the largest characteristic velocity occurs at the leading edge in the vicinity of the laminar separation bubble. Significant characteristic velocity is also evident in the turbulent boundary layer of the plate and near the trailing edge. Close inspection of Figure 4(b) reveals that the characteristic frequency ω_s of the turbulent fluctuations is greater than 1kHz everywhere within the turbulent boundary layer and near-wake of the flat plate. The characteristic length scale l_s of the turbulent fluctuations is zero on the surface of the flat plate and then increases to a maximum approximately mid way through the turbulent boundary layer. The length scale then decreases slightly further out in the turbulent boundary layer. Figure 4 also reveals that the characteristic length scale of the turbulent fluctuations increases downstream of the trailing edge. These distributions of the characteristic velocity, frequency and length scales are then combined with equation (19) to compute the turbulent velocity cross spectra.

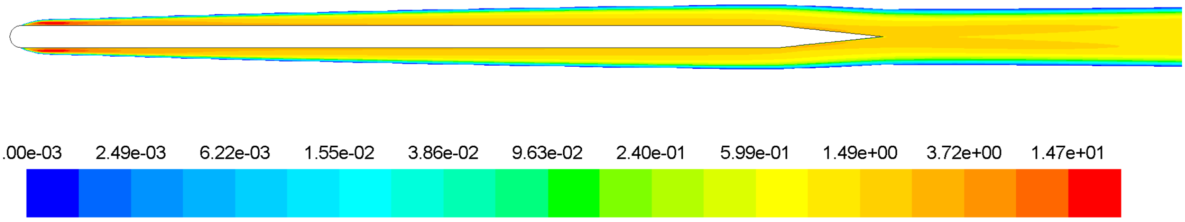

(a) Turbulent kinetic energy, k

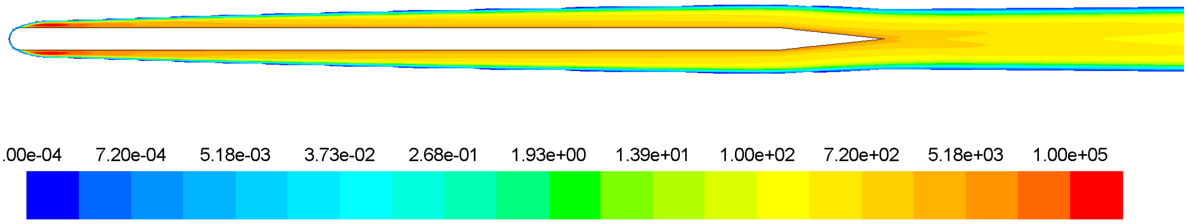

(b) Turbulent dissipation rate, ε

Figure 2 – Turbulent properties in the flow past the sharp-edged flat plate

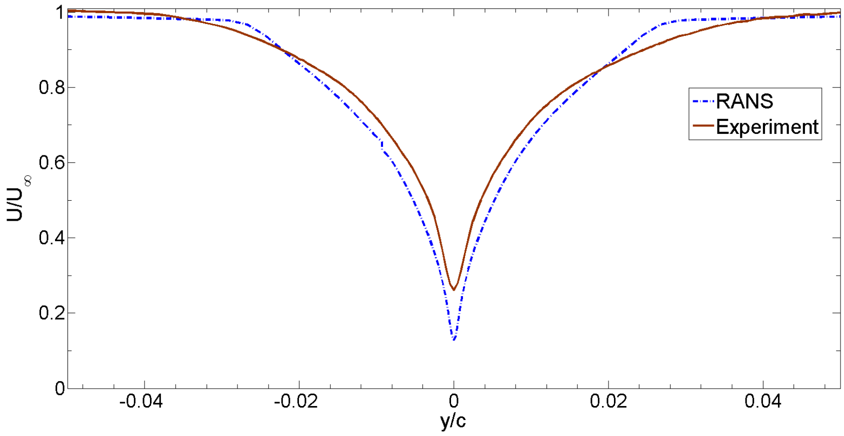

(a) Normalised mean velocity, U/U_∞

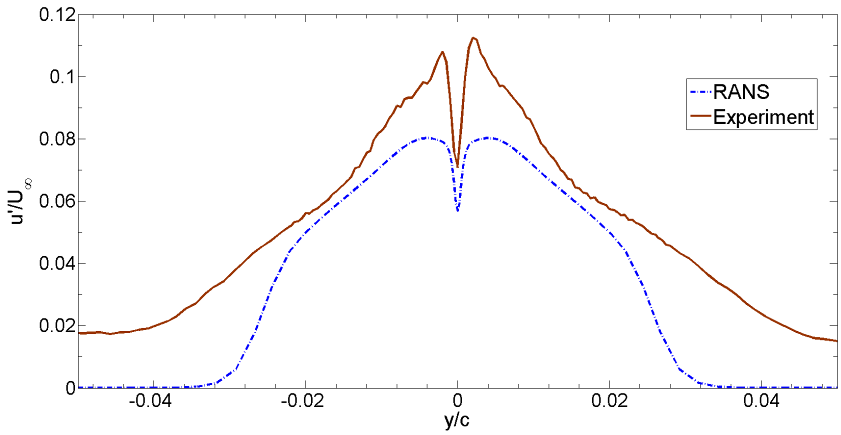

(b) Normalised rms velocity, $u'_{\mathrm{rms}}/U_\infty$

Figure 3 – Normalised velocity in the near wake of the trailing edge

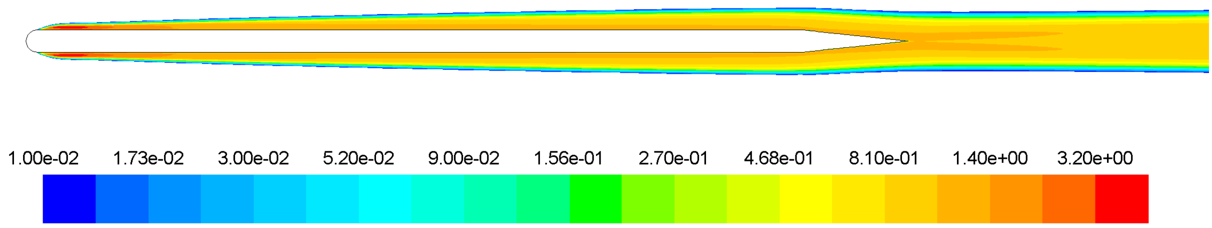

(a) Characteristic velocity u_s

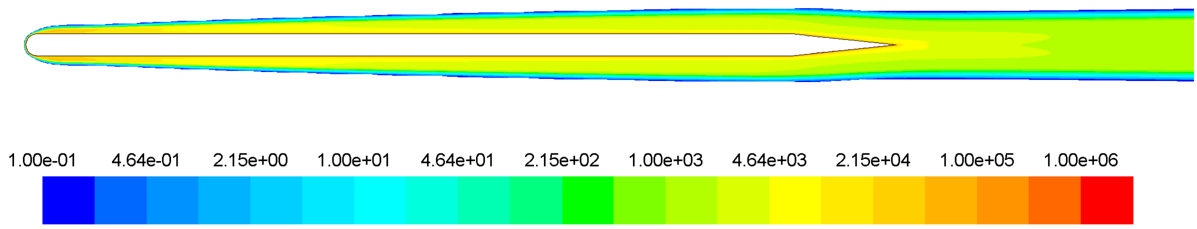

(b) Characteristic frequency ω_s

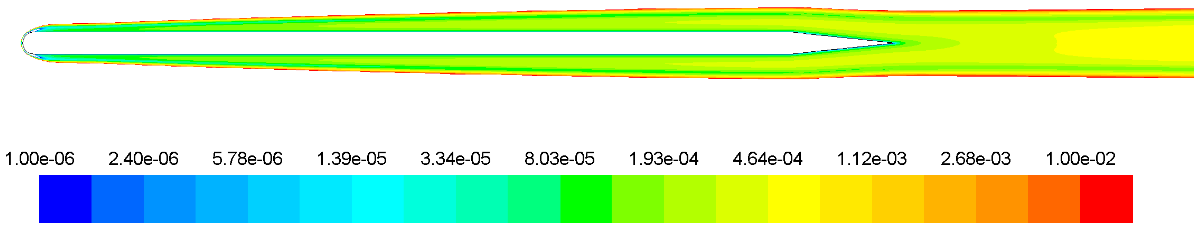

(c) Characteristic length scale l_s

Figure 4 – Distributions of u_s, ω_s and l_s used in the RSNM

3.2 Acoustic Results

The turbulent velocity cross spectra obtained in the preceding section are then applied to the normalised far-field pressures of equation (17) to predict the far-field power spectral density. As only a two-dimensional CFD simulation was performed, the following procedure was adopted to predict the far-field PSD of the 450mm span:

1. The span was divided into 450 equal segments of 1mm;
2. The far-field PSD of one segment was calculated from equations (14) and (15);
3. The far-field PSD was then modified to account for scattering by the entire span using the following correction (23)

$$\mathrm{PSD}_t = \mathrm{PSD}_s + \mathrm{PSD}_c \tag{21}$$

where PSD_t and PSD_s are the power spectral density for the entire span and simulated span, respectively, and PSD_c is a correction given by

$$\mathrm{PSD}_c = \begin{cases} 10\log(N), & \frac{L_c'}{L_s} \leq \frac{1}{\sqrt{\pi}} \\ 10\log\left(\frac{L_c'}{L_s}\right) + 10\log\left(\sqrt{\pi}N\right), & \frac{1}{\sqrt{\pi}} < \frac{L_c'}{L_s} < \frac{N}{\sqrt{\pi}} \\ 20\log(N), & \frac{L_c'}{L_s} \geq \frac{N}{\sqrt{\pi}} \end{cases} \tag{22}$$

where N is the total number of segments. L_s is the length of the simulated span and L_c' is the spanwise coherence length and is approximated by $L_c' = 2.1U_{\mathrm{con}}/\omega$ (24).

Figure 5 compares the power spectral density of the far-field sound predicted with the hybrid RANS-BEM technique to the experimental measurements of Moreau et al. (22). The far-field sound predicted with the proposed RANS-BEM technique compares favourably with the experimental results at frequencies above approximately 600 Hz. As the frequency decreases the difference between the numerical prediction and experimental measurement increases. The interaction between the leading edge and incoming turbulent gusts is believed to dominate the low frequency noise generated by the flat plate. The present RANS-BEM technique is unable to resolve these turbulence gusts. Hence it cannot accurately predict the low frequency component of the far-field sound.

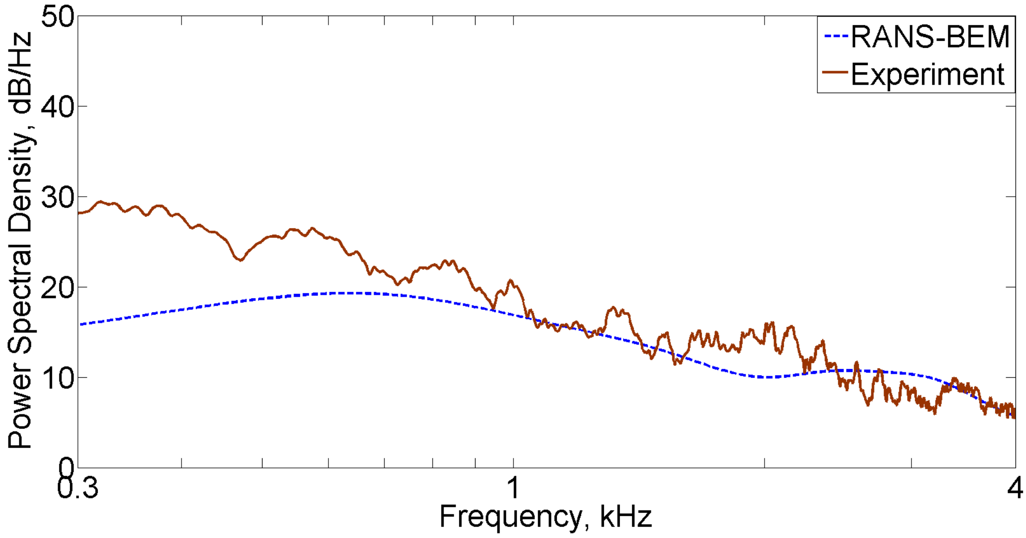

Figure 5 – Comparison of numerical and experimental far-field sound

4. SUMMARY

A hybrid RANS-BEM technique has been proposed to predict the flow induced noise generated by turbulent flow over a body. The method is based on mean flow field data produced by a steady state RANS simulation of turbulent flow over a body. This flow field data is then processed by a statistical noise model to estimate the turbulent velocity cross spectra. These turbulent velocity cross spectra are then combined with a BEM model to predict the scattering and diffraction of the flow induced sound by the body. This hybrid RANS-BEM technique has been applied to predict the flow induced noise generated by turbulent flow over a sharp-edged plate at a Reynolds number based on the chord of $Re_c = 2.0 \times 10^5$ and a Mach number of $M = 0.044$. The near-wake mean and rms velocity profiles predicted with the RANS CFD simulation compares favourably with published experimental measurements. The far-field sound predicted with the proposed RANS-BEM technique was observed to agree well with the experimental results at higher frequencies.

REFERENCES

1. Lighthill MJ. On sound generated aerodynamically, I. General theory. Proc Roy Soc A. 1952;211:564–587.

2. Lighthill MJ. On sound generated aerodynamically, II. Turbulence as a source of sound. Proc Roy Soc A. 1954;222:1–32.

3. Curle N. The influence of solid boundaries upon aerodynamic sound. Proc Roy Soc Lon A. 1955;231:505–514.

4. Gloerfelt X, Pérot F, Bailly C, Juvé D. Flow-induced cylinder noise formulated as a diffraction problem for low Mach numbers. J Sound Vib. 2005;287:129–151.

5. Martínez-Lera P, Schram C. Correction techniques for the truncation of the source field in acoustic analogies. J Acoust Soc Am. 2008;124:3421–3429.

6. Ffowcs Williams JE, Hall LH. Aerodynamic sound generation by turbulent flow in the vicinity of a scattering half plane. J Fluid Mech. 1970;40:657–670.

7. Wang M, Moreau S, Iaccarino G, Roger M. LES prediction of wall-pressure fluctuations and noise of a low-speed airfoil. Int J Aero Acoust. 2009;8:177–198.

8. Khalighi Y, Mani A, Ham F, Moin P. Prediction of sound generated by complex flows at low Mach numbers. AIAA J. 2010;48(2):306–316.

9. Ewert R. Broadband slat noise prediction based on CAA and stochastic sound sources from a fast random particle-mesh (RPM) method. Comput Fluids. 2008;37:369–387.

10. Casalino D, Barbarino M. Stochastic Method for Airfoil self-noise computation in frequency domain. AIAA J. 2011;49:2453–2469.

11. Ewert R, Dierke J, Siebert A, Appel C, Siefert M, Kornow O. CAA broadband noise prediction for aeroacoustic design. J Sound Vib. 2011;330:4139–4160.

12. Albarracin CA, Doolan CJ, Jones RF, Hansen CH, Brooks LA, Teubner MD. A RANS-based statistical noise model for trailing edge noise. In: 18th AIAA/CEAS Aeroacoustics Conference (33rd AIAA Aeroacoustics Conference). Colorado, USA; 2012.

13. Amiet K R. Noise due to turbulent flow past a trailing edge. J Sound Vib. 1976;47:387–393.

14. Chandiramani KL. Diffraction of evanescent waves, with applications to aerodynamically scattered sound and radiation from unbaffled plates. J Acoust Soc Am. 1974;55:19–29.

15. Lee YT, Blake WK, Farabee TM. Modeling of wall pressure fluctuations based on time mean flow field. J Fluids Eng. 2005;127:233–240.

16. Ostertag JSD, Guigati S, Guidati G, Wagner S, Wilde A, Kalitzin N. Prediction and measurement of airframe noise on a generic body. In: 6th AIAA/CEAS Aeroacoustics Conference. Lahaina, Hawaii, USA; 2000.

17. Crighton DG. Goals for computational aeroacoustics. In: Lee D, Sternberg RL, Schultz MH, editors. Computational Acoustics: Algorithms and Applications. Elsevier; 1988.

18. Marburg S, Nolte B, editors. Computational Acoustics of Noise Propagation in Fluids. Springer, Berlin, Germany; 2008.

19. Kirkup SM. The Boundary Element Method in Acoustics. Integrated Sound Software; 1998.

20. Oberai A, Roknaldin F, Hughes TJR. Computation of trailing edge noise due to turbulent flow over an airfoil. AIAA J. 2002;40:2206–2216.

21. Moreau D, Brooks L, Doolan C. Broadband trailing edge noise from a sharp-edged strut. J Acoust Soc Am. 2011;129:2820–2829.

22. Moreau D, Brooks L, Doolan C. The effect of boundary layer type on trailing edge noise from sharp-edged flat plates at low-to-moderate Reynolds number. J Sound Vib. 2012;331:3976–3988.

23. Seo JH, Moon YJ. Aerodynamic noise prediction for long-span bodies. J Sound Vib. 2007;306(3-5):564–579.

24. Corcos GM. The structure of the turbulent pressure field in boundary-layer flows. J Fluid Mech. 1964;18:353–378.